Au-doped PtCo/C catalyst preventing Co leaching for proton exchange membrane fuel cells

Juhyuk Choi[a], Jinwon Cho[b], Chi-Woo Roh[a], Beom-Sik Kim[a], Min Suk Choi[a], Hojin Jeong[a], Hyung Chul Ham[b],*, Hyunjoo Lee[a],*

[a] *Department of Chemical and Biomolecular Engineering, Korea Advanced Institute of Science and Technology, Daejeon 34141, Republic of Korea*
[b] *Fuel Cell Research Center, Korea Institute of Science and Technology (KIST), Seoul 02792, Republic of Korea*

ARTICLE INFO

Keywords:
PEMFC
Leaching
Durability
Cobalt
Gold

ABSTRACT

Proton exchange membrane fuel cells (PEMFCs) are promising mobile power supply systems, and operate without noise or polluting emissions. Because the oxygen reduction reaction (ORR) at the cathode suffers from high overpotential and sluggish kinetics, many catalysts have been developed in efforts to enhance activity and durability for the ORR. However, most of them have complicated synthetic procedures which cannot be scaled-up easily, and have only been tested in a half-cell. High activity in a half-cell does not necessarily guarantee better performance in a single-cell. In this work, we synthesized an Au-doped PtCo/C catalyst using a simple method of gas-phase reduction and subsequent galvanic replacement, and its activity and durability were tested in a single-cell. When current densities were compared at 0.6 V after a durability test of 30,000 cycles in 0.6–1.0 V, the values were 1.40, 0.81, and 0.63 A cm^{-2} for the Au-doped PtCo/C, acid-treated PtCo/C, and commercial Pt/C catalysts, respectively. Co leaching was much less in the Au-doped PtCo/C. Density functional theory (DFT) calculations confirmed that surface oxygen species bound more weakly at the catalyst surface and migration of a Co atom (Co segregation) to the surface was suppressed in the presence of Au. This facile method can provide a more realistic strategy to design better ORR catalysts for PEMFC application.

1. Introduction

Proton exchange membrane fuel cells (PEMFCs) efficiently provide electricity from hydrogen fuel. PEMFC vehicles such as NEXO or Mirai are already available in the market. Those fuel cell vehicles can also serve as a mobile power supply without polluting emissions. Autonomous cars with high electric power demand would make fuel cell vehicles more suitable than pure battery powered vehicles. However, PEMFCs still require massive amounts of Pt catalyst to promote the sluggish oxygen reduction reaction (ORR) [1–4]. As the market for PEMFC vehicles increases, the high price and limited supplies of Pt could be a serious obstacle hindering market expansion. Thus, developing a catalyst with higher activity and durability while minimizing the use of Pt is urgently required. Various shape- and composition-controlled nanoparticles were synthesized using colloidal synthesis method, but they often suffer from complicated synthetic procedures, small synthesis amount in a milligram scale, and the removal of surface-capping organic agents used during the syntheses [5–8]. The synthesis method which is facile and easy to scale-up is preferred for commercial applications.

Forming Pt-based alloys with various transition metals such as Mn, Fe, Co, Ni, Cu, Zn has been extensively reported to enhance activity for the ORR [9–18]. In the Pt-TM (Pt-transition metal) alloys, the Pt electronic structure is modified by the underlying transition metal, inducing a decrease in the binding energy of oxygen species and increasing ORR activity [19–23]. Specifically, PtCo alloy catalysts have demonstrated high activity and good durability in half-cell and single-cell tests [24–28]. Because high activity in a half-cell does not guarantee high activity in a single-cell, the catalyst should be tested in both conditions [29]. It is known that Mirai uses PtCo catalysts [30]. However, Pt-TM alloy catalysts typically suffer from leaching. The transition metal is easily oxidized in acidic conditions and is leached out from nanoparticles during the ORR, leading to poorer activity and durability over extended operating times. The leached transition metal can also contaminate the proton exchange membrane, degrading single-cell performance significantly [31].

Many studies have attempted to enhance the activity and durability of the Pt-TM catalysts. The transition metal located on the surface has been intentionally removed by cyclic voltammetry (CV), acid treatment, or thermal dealloying, forming a core-shell structure that consists
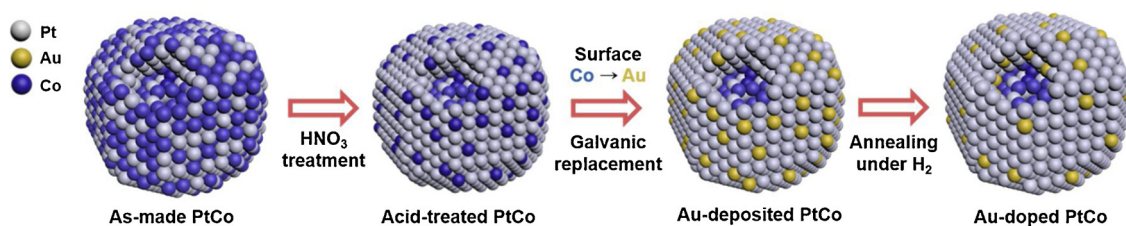
Fig. 1. Schematic illustration of the catalyst preparation.

Table 1
Properties of nanoparticle catalysts before and after accelerated durability tests (ADTs) in a half-cell (hc) and a single-cell (sc).

| Catalysts	Average particle size (nm)	Atomic ratio (%)			
		ICP (Pt:Co:Au)	EDS (Pt:Co:Au)	XPS (Pt:Co:Au)	XPS (Pt°:Pt^{2+}:Pt^{4+})
as-made PtCo/C	5.6 ± 2.9	68:32:0	69:31:0	18:82:0	63:22:15
acid-treated PtCo/C	4.4 ± 1.4	73:27:0	76:24:0	82:18:0	71:21:8
Au-deposited PtCo/C	4.4 ± 1.5	75:23:2	77:21:2	77:19:3	62:20:18
Au-doped/C	4.4 ± 1.3	74:24:2	77:21:2	82:17:1	65:27:8
acid-treated PtCo/C after ADT$_{hc}$	8.7 ± 4.9	N/A	97:3:0	100:0:0	60:25:15
Au-doped PtCo/C after ADT$_{hc}$	5.7 ± 2.5	N/A	84:15:1	100:0:0	68:23:9
acid-treated PtCo/C after ADT$_{sc}$	14.7 ± 12.3	N/A	94:6:0	100:0:0	55:19:26
Au-doped PtCo/C after ADT$_{sc}$	8.1 ± 3.0	N/A	87:12:1	90:9:1	60:28:12
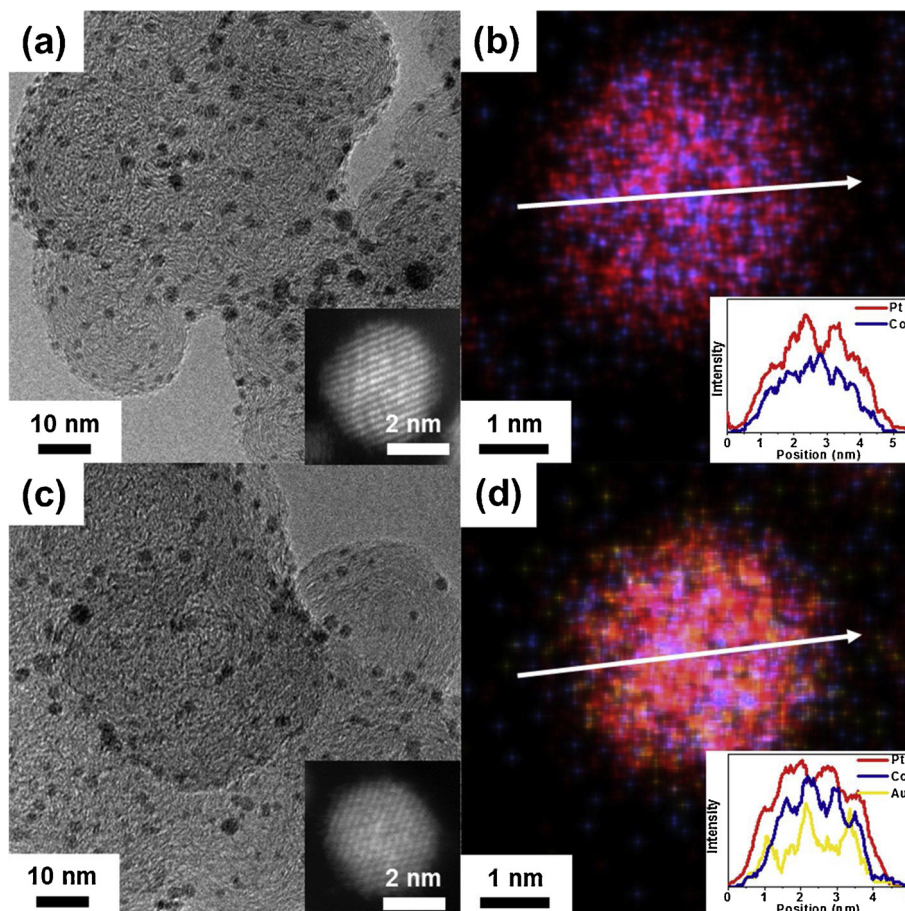
Fig. 2. TEM images (inset: HAADF-STEM), EDS mapping (inset: elemental line-scanning images, Pt: red, Co: blue, Au: yellow) for the (a, b) acid-treated PtCo/C and (c, d) Au-doped PtCo/C (For interpretation of the references to colour in this figure legend, the reader is referred to the web version of this article).gr2

of a transition metal core and a Pt thin shell [32–34]. Or, a core-shell structure has been formed by depositing a Pt thin layer on Pd-TM, Ir-TM, or Au cores by the underpotential deposition (UPD) method [35–38]. But the transition metal atoms in the alloys can be easily segregated due to lattice mismatch or difference in surface energy [39,40]. Moreover, when oxygen species, which are ORR intermediates, are adsorbed on the Pt-TM surface, segregation of the transition metal atoms is accelerated [41]. Preventing the segregation and leaching of the transition metal atoms in the Pt-TM catalysts is an important objective.
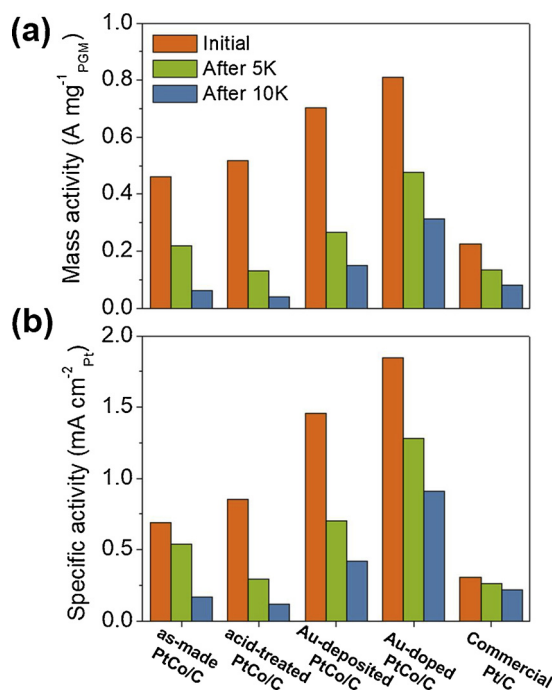
Fig. 3. The changes in (a) mass activity and (b) specific activity at 0.9 V_{RHE} after the durability tests for the as-made PtCo/C, acid-treated PtCo/C, Au-deposited PtCo/C, Au-doped PtCo/C, and commercial Pt/C. The durability was tested in 0.6–1.0 V_{RHE} at a scan rate of 100 mV s^{-1} in O_2-saturated 0.1 M HClO$_4$ solution.

It was reported that adding Au to Pt-based catalysts can significantly enhance activity and durability by more easily eliminating oxygen species from the Pt surface or preventing Pt oxidation at high voltages [42]. Au-based core-Pt shell, Au clusters deposited on Pt/C, or Au-doping of PtCu have been reported [43–47]. However, the Au amounts were often too high, the synthesis methods were too complicated to scale-up, and single-cell test results have rarely been reported.

In this work, we synthesized a Au-doped PtCo/C catalyst by gas-phase reduction and subsequent galvanic replacement at gram-scale. The prepared catalyst was tested in a half-cell and a single-cell, and showed high activity and durability per unit mass of precious metal. The oxygen binding energy and Co segregation energy in the absence or presence of Au in a Pt shell were compared using density functional theory (DFT) calculations.

2. Experimental

2.1. Synthesis of Au-doped PtCo/C catalyst

All the chemicals were used as purchased without further purification: platinum acetylacetonate (Pt(acac)$_2$, Sigma-Aldrich, 97%), cobalt acetylacetonate (Co(acac)$_2$, Sigma-Aldrich, 97%), carbon (Vulcan® XC-72R, Cabot), potassium gold chloride (KAuCl$_4$, Sigma-Aldrich, 98%), nitric acid (HNO$_3$, SAMCHUN, 60%), isopropyl alcohol (IPA, Junsei, 99.7%), acetone (SAMCHUN, 99.5%), 5 wt% Nafion® perfluorinated resin solution (Sigma-Aldrich), perchloric acid (HClO$_4$, Sigma-Aldrich, 70%), commercial Pt/C (Johnson Matthey, 20 wt%). The deionized water (18 MΩ cm^{-1}) was prepared with Human power II$^+$.

1.05 mmol of Pt(acac)$_2$ and 0.53 mmol of Co(acac)$_2$ were dissolved in 50 mL of acetone, then 1 g of carbon (Vulcan® XC-72R) was added into the solution. The mixture was dried, the obtained black powder
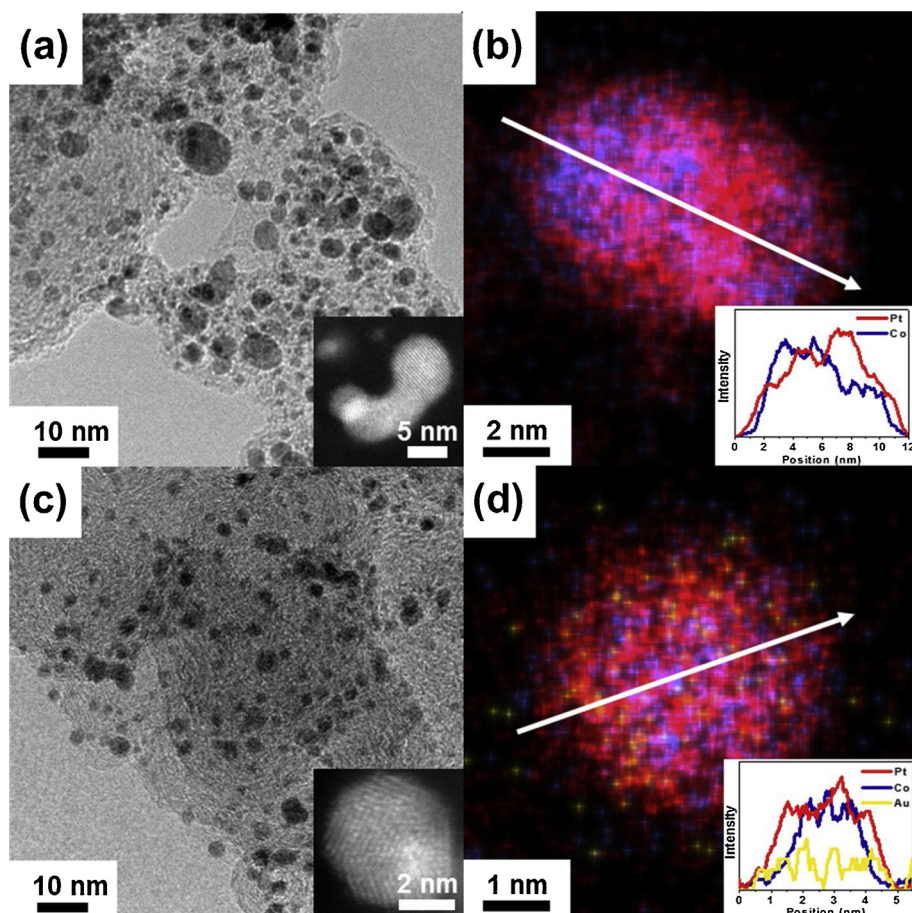

Fig. 4. TEM (inset: HAADF-STEM) and EDS mapping (inset: elemental line-scanning, Pt: red, Co: blue, Au: yellow) images of (a, b) the acid-treated PtCo/C and (c, d) the Au-doped PtCo/C after 10,000 cycles in the half-cell durability tests (For interpretation of the references to colour in this figure legend, the reader is referred to the web version of this article).
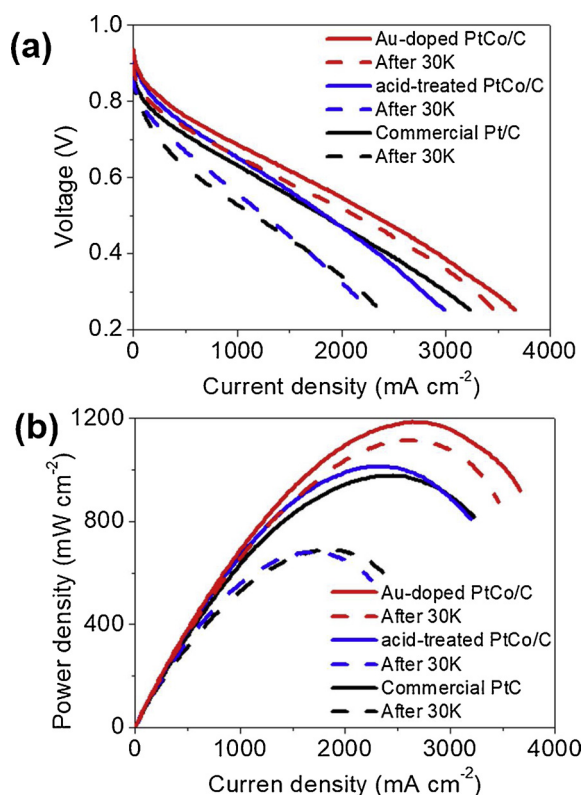
(a)

(b)

Fig. 5. I–V polarization curves of single-cells for the acid-treated PtCo/C, the Au-doped PtCo/C, and the commercial Pt/C catalysts. The initial performance is shown by solid lines and the performance after 30,000 cycles is shown with dashed lines. The durability tests were conducted by repeating CVs in 0.6–1.0 V at 100 mV s^{-1} in Ar flow at the cathode with 100% RH.

was reduced under H_2/N_2 flow (20:180 sccm) at 500 °C for 2 h, then annealed under N_2 flow at 500 °C for 5 h (as-made PtCo/C). The Co oxide layer at the surface was eliminated by etching the as-made PtCo/C in 0.5 mM of HNO_3 solution for 10 min, then the solid powder was washed with deionized water and dried at 80 °C (acid-treated PtCo/C). Au was deposited onto the PtCo/C using galvanic replacement. 1 g of acid-treated PtCo/C was dispersed in 0.5 mM of Ar-saturated HNO_3 solution. $KAuCl_4$ was added into the solution, resulting in an Au concentration of 0.05 mM. After stirring for 10 min at 800 rpm, the solid powder was washed with deionized water and dried at 80 °C (Au-deposited PtCo/C). The dried powder was annealed under H_2/N_2 flow (8:192 sccm) at 200 °C for 2 h (Au-doped PtCo/C).

2.2. Electrochemical measurements: half-cell and single-cell

The electrochemical half-cell tests were performed in a three-electrode cell with a CHI 760E potentiostat at 25 °C. The working electrode was a rotating ring disk electrode of glassy carbon (Pine, area: 0.247 cm^2). The counter electrode was a coiled platinum wire, and the reference electrode was 3 M NaCl saturated Ag/AgCl. All the potentials in the half-cell tests were reported versus a reversible hydrogen electrode (RHE), which was obtained by hydrogen oxidation and evolution in a H_2-saturated 0.1 M $HClO_4$ solution using a Pt rotating disk electrode. The catalyst powder was mixed in deionized water, IPA, and 5 wt% Nafion® ionomer, and sonicated in an ultrasonic bath for 20 min. The catalyst ink was loaded on the working electrode and dried. The Pt loading was 12.1 μg_{Pt} cm^{-2}. The catalyst was activated by repeating 50 cycles of CV between 0.05 V_{RHE} and 1.0 V_{RHE} in an Ar-saturated 0.1 M $HClO_4$ solution at 100 mV s^{-1}. The electrochemical surface area (ECSA) was evaluated by averaging the integrated H_{UPD} charges using 210 μC cm$_{Pt}^{-2}$. Linear sweep voltammetry (LSV) results were collected between

0.05 V_{RHE} and 1.1 V_{RHE} to the anodic scan direction in O_2-saturated 0.1 M $HClO_4$ solution at 10 mV s^{-1} and 1600 rpm. The ORR mass and specific activities were estimated using the Koutecky-Levich equation at 0.9 V_{RHE} from the LSV curves after iR correction. Durability was tested by performing an accelerated degradation test (ADT$_{half\ cell,\ hc}$) between 0.6 V_{RHE} and 1.0 V_{RHE} for 5000 or 10,000 cycles in O_2-saturated 0.1 M $HClO_4$ at 100 mV s^{-1}.

Single-cell tests were performed on a SMART2 PEM fuel cell station (WonA-Tech). The membrane electrode assemblies (MEAs) were fabricated by a catalyst coated membrane (CCM) method. The cathode was prepared using acid-treated PtCo/C, Au-doped PtCo/C, or commercial Pt/C with a Pt loading of 0.2 mg cm^{-2}. The anode was made with commercial Pt/C in all cases with a Pt loading of 0.2 mg cm^{-2}. The catalyst ink, which was prepared by mixing the catalysts, deionized water, IPA, and Nafion® ionomer, were directly coated on a Nafion 212 membrane (5 cm^2) using a spray gun. The cell temperature was 80 °C. 200 sccm H_2 was fed to the anode and 600 sccm O_2 was fed to the cathode with 100% relative humidity (RH). After activation, I–V polarization curves were obtained from open-circuit voltage to 0.25 V at 1.6 bar of back pressure. The ADT$_{single-cell,\ sc}$ was conducted at 100 mV s^{-1} between 0.6 V and 1.0 V for 30,000 cycles with a flow of 200 sccm H_2 in the anode and 75 sccm Ar in the cathode with 100% RH.

2.3. Characterizations

Transmission electron microscopy (TEM) images were taken by Tecnai TF30 ST operated at 300 kV. High angle annular dark field scanning TEM (HAADF-STEM) images were obtained using a Titan double Cs-corrected TEM (Titan cubed G2 60–300) operated at 200 kV. Elemental mapping with energy dispersive spectroscopy (EDS) was performed on a Titan double Cs-corrected TEM operated at 80 kV. The surface oxidation states of the catalysts were evaluated with X-ray photoelectron spectroscopy (XPS, K-alpha, Thermo VG Scientific). Cross sectional images of the MEA were obtained by scanning electron microscopy (SEM, Magellan400). The metal content in the catalysts was determined by inductively coupled plasma optical emission spectroscopy (ICP-OES, Agilent 7700S). The concentration of leached ions in the electrolyte was estimated using inductively coupled plasma mass spectroscopy (ICP-MS, Agilent 720). Extended X-ray absorption fine structure (EXAFS) spectra were obtained using 8C Nano XAFS beamline of Pohang Light Source (PLS).

2.4. DFT calculations

The calculations were performed using spin polarized density functional theory (DFT) within the Perdew − Burke − Ernzerhof (PBE), as implemented in the Vienna ab-initio simulation package (VASP) [48,49]. The projector augmented wave (PAW) method with a plane-wave basis set was employed to describe the interaction between core and valence electrons [50]. An energy cutoff of 400 eV was applied for the planewave expansion of the electronic eigenfunctions. A $(3 \times 3 \times 1)$ Monkhorst-Pack mesh of k points was used to calculate geometries and total energies for the Brillouin zone integration [51]. A supercell slab was built for the pure Pt catalyst with a face-centered cubic Pt (111) surface composed of a hexagonal (3×3) surface unit cell with six atomic layers, each of which contained nine atoms. A (2×2) six-layer ordered PtCo (110) slab was also constructed with a tetragonal P4/mmm space group and bulk lattice parameters of a = 2.68 Å, c = 3.77 Å. Here, the (110) facet was chosen because it has been reported to be the most exposed surface among the low-index facets in Pt-TM ordered structures [52,53]. Then, all of the Co atoms in the top three surface layers of an ordered PtCo (110) slab were replaced by Pt atoms to produce pure Pt skinlayers supported on a PtCo (110) substrate. Next, Au-doped Pt skinlayers supported on the ordered PtCo (110) substrate were prepared by substituting a single Pt atom in each Pt skinlayer with an Au atom. The slab was separated from its periodic
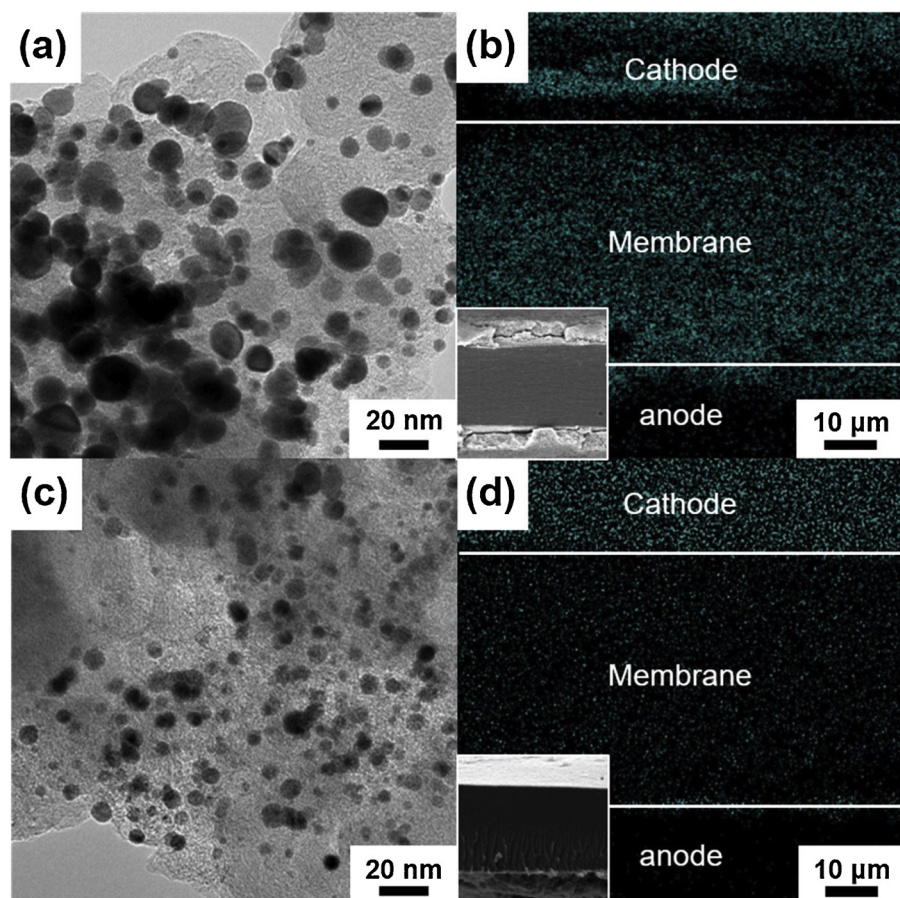
Fig. 6. TEM images of the catalysts and cross-sectional SEM-EDS mapping images of the MEAs (blue: Co) for (a, b) the acid-treated PtCo/C and (c, d) the Au-doped PtCo/C after 30,000 cycles of the durability tests in single-cells (inset: SEM images) (For interpretation of the references to colour in this figure legend, the reader is referred to the web version of this article).
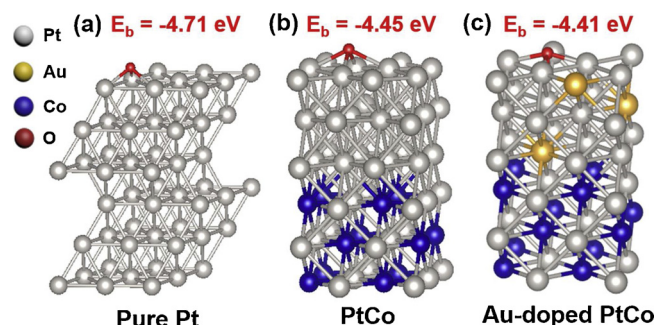

Fig. 7. Models used for DFT calculations; (a) pure Pt(111), (b) ordered PtCo (110) with a tetragonal P4/mmm space group, and (c) Au-doped Pt skinlayers supported on the ordered PtCo (110). The oxygen binding energies (E_b) calculated for each model are shown together. (Pt: grey, Au: yellow, Co: blue, O: red) (For interpretation of the references to colour in this figure legend, the reader is referred to the web version of this article).

images in the vertical direction by a vacuum space corresponding to seven atomic layers. While the bottom two layers were fixed at corresponding bulk positions, the upper four layers were fully relaxed using the conjugate gradient method until the residual forces on all the constituent atoms became smaller than 5×10^{-2} eV/A.

3. Results and discussion

3.1. Au-doped PtCo/C catalyst

The 'as-made PtCo/C' catalyst was synthesized by reducing Pt (acac)$_2$ and Co(acac)$_2$ precursors deposited on the carbon support under H$_2$ flow at 500 °C. Then a mild acid treatment was performed by

dispersing the as-made sample in 0.5 mM HNO$_3$ for 10 min to etch the surface Co oxide ('acid-treated PtCo/C'). Au was deposited on the acid-treated sample by galvanic replacement ('Au-deposited PtCo/C'). Then the catalyst was annealed under H$_2$ flow at 200 °C ('Au-doped PtCo/C'). The overall synthesis scheme is shown in Fig. 1. The nanoparticle sizes, atomic composition, and surface properties of each catalyst are shown in Table 1. The as-made sample could be prepared in a gram-scale from one batch as shown in Figure S1. The average nanoparticle size estimated from TEM images was 5.6 ± 2.9 nm. It also contained large particles with an approximate size of 10 nm, and they are considered to be Co oxides. The overall atomic composition was measured by both ICP and EDS, and the results were similar, showing 68% Pt and 32% Co from ICP versus 69% Pt and 31% Co from EDS. However, the surface compositions differed, with 18% Pt and 82% Co, indicating that Co was mainly located at the surface. After the acid treatment, the surface Co oxide was leached, and the surface composition of Pt increased to 82%. The nanoparticle size decreased to 4.4 ± 1.4 nm, and the HAADF-STEM image in Fig. 2 shows that Pt and Co are distributed throughout the particle. The XRD data in Figure S2 also confirms that PtCo alloy phase was formed. The Pt content in the acid-treated PtCo/C was 20.1 wt%.

Au was deposited on the acid-treated PtCo/C catalyst by galvanic replacement at an optimized condition of 0.05 mM of KAuCl$_4$, 10 min, and 25 °C. Figure S3 shows that well-dispersed uniform nanoparticles were formed at the optimized condition, whereas the other conditions often produced large (≥ 10 nm) Au particles. Au content was as low as 2 atomic %. The average particle size showed little difference even after Au deposition. The Au content at the surface was a little higher than the overall Au composition, which was 3 atomic %. The Au-deposited PtCo/C catalyst was annealed under H$_2$ flow at 200 °C. The surface Au composition changed into 1 atomic %. Au atoms moved inwardly during annealing, while the particle size and overall composition
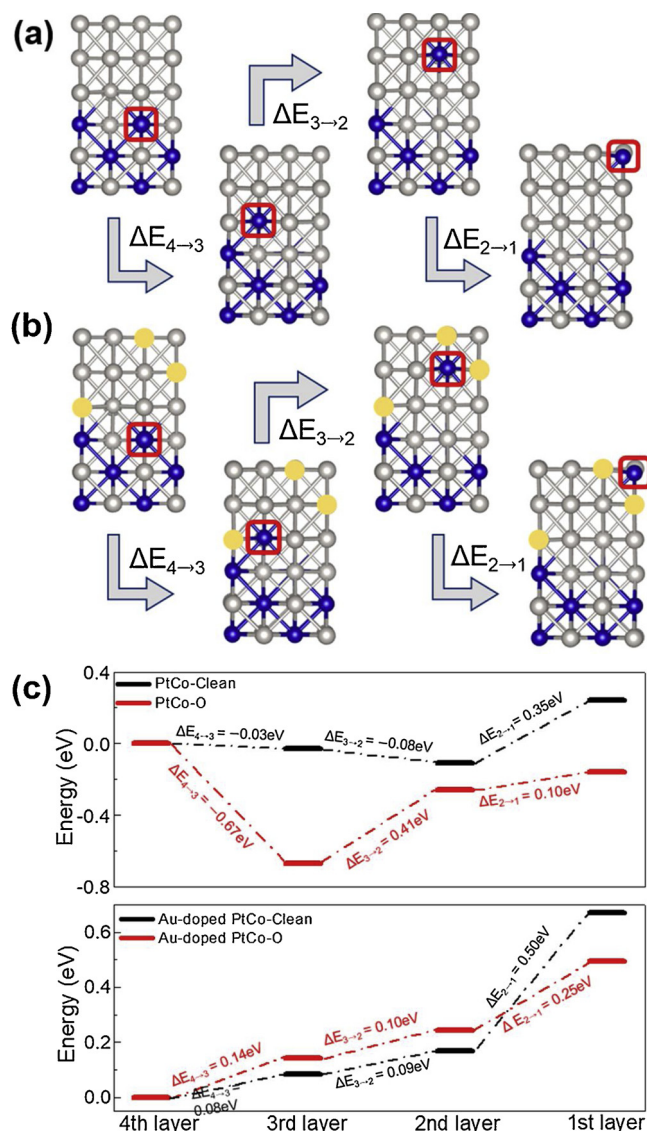
Fig. 8. Schematic atomic configuration of Co segregation in (a) PtCo and (b) Au-doped PtCo. (c) The energy variation as a function of Co position in PtCo (upper) and Au-doped PtCo (lower) slabs at clean and oxygen conditions.

showed no change. Fig. 2 presents TEM, HAADF-STEM, and EDS mapping images of the Au-doped PtCo/C catalyst. Au was uniformly distributed throughout the particle. Figure S4 shows EXAFS spectra of Au L3 edge. The intensity of Au-Au peaks at 2.6 Å and 2.8 Å diminished significantly after H_2 annealing, indicating that Au was atomically dispersed on the Au-doped PtCo/C catalyst. The change of oxygen binding energy on the acid-treated PtCo/C and Au-doped PtCo/C were evaluated by O_2-TPD method as shown in Figure S5. The oxygen desorption temperature were slightly decreased on the Au-doped PtCo/C catalysts. The oxygen bonding were weakened by the Au-doping.

3.2. Half-cell and single-cell tests

Activity and durability of the various catalysts for the ORR were tested in a half-cell. Figure S6 shows CV and LSV curves measured in 0.1 M $HClO_4$ solution. The oxygen species reduction peak in the CVs was shifted upon Au doping from 0.75 V_{RHE} for the acid-treated PtCo/C to 0.77 V_{RHE} for the Au-doped PtCo/C. This shift indicates that the overpotential for ORR decreased after Au doping. The changes in ECSA, mass activity, and specific activity at 0.9 V_{RHE} after the durability tests, which were performed by repeating CVs in 0.6–1.0 V_{RHE} at 100 mV s^{-1},

are summarized in Figure S7 and Fig. 3. When the mass activity was normalized by the total mass of Pt and Au, the initial activity increased from 0.52 A mg$_{Pt}^{-1}$ for the acid-treated catalyst to 0.81 A mg$_{PGM}^{-1}$ for the Au-doped catalyst. More importantly, durability was enhanced significantly. After 10,000 cycles, the Au-doped catalyst presented a mass activity of 0.31 A mg$_{PGM}^{-1}$, while the value for the acid-treated catalyst or commercial Pt/C catalyst was 0.04 A mg$_{Pt}^{-1}$ or 0.08 A mg$_{Pt}^{-1}$, respectively. After the durability test in a half-cell, the nanoparticles were observed by TEM as shown in Fig. 4. The size increased greatly to 8.7 ± 4.9 nm for the acid-treated catalyst. Most of the Co was leached out, resulting in a final composition of 97% Pt and 3% Co. The surface consisted of 100% Pt. EDS mapping image also confirmed the presence of the Pt shell. For the Au-doped catalyst, however, the nanoparticle sized increased less, to 5.7 ± 2.5 nm, and the final composition was 84% Pt, 15% Co, and 1% Au. The Co ions leached into the electrolyte solution after 10,000 cycles were detected using ICP-MS. The concentration of Co was 3.2 ppb for the acid-treated catalyst and 1.8 ppb for the Au-doped catalyst. The Co leached much less in the presence of Au. The percentage of metallic Pt (Pt°) was compared. Although it decreased from 71% to 60% after 10,000 cycles for the acid-treated catalyst, for the Au-doped catalyst it increased from 65% to 68%. The Au doping helped to preserve metallic surface Pt during the ORR. The catalysts turnover frequency (TOF) were also calculated using the ORR current at 0.9 V_{RHE} and ECSA, as shown in Figure S8. The Au-doped PtCo/C showed a higher initial TOF (1.67 s^{-1}) than the acid-treated PtCo/C (1.01 s^{-1}) and the commercial Pt/C (0.50 s^{-1}). After 10,000 cycles, the TOF of acid-treated PtCo/C and Au-doped PtCo/C decreased by 75% and 22%, respectively.

Next, the single-cell performances of the acid-treated PtCo/C, Au-doped PtCo/C, and commercial Pt/C were tested as shown in Fig. 5. The Pt loading was 0.2 mg cm^{-2} at both cathode and anode for all the catalysts. I–V and power density curves were obtained in H_2/O_2 flow (200/600 sccm) at 80 °C with 100% RH. The current densities at 0.8 V were 0.23, 0.31, and 0.11 A cm^{-2} for the acid-treated, Au-doped, and commercial Pt catalysts, respectively. Typically, the performance in the low current density region is determined by the activity of the catalysts [54]. As expected from the half-cell test results, the Au-doped catalyst showed the highest current density, while the commercial catalyst showed much poorer current density. When the current densities were compared at 0.6 V, the values were 1.31, 1.63, and 1.20 A cm^{-2} for the acid-treated, Au-doped, and commercial Pt catalysts, respectively. The acid-treated catalyst only showed a current density comparable to the commercial catalyst. The ohmic resistance often determines the mid-current density region [54]. The Co leached from PtCo nanoparticles might contaminate the membrane or degrade the proton conductivity. The maximum power densities were 1.02, 1.19, and 0.98 W cm^{-2} for the acid-treated, Au-doped, and commercial Pt catalysts, respectively. The Au-doped catalyst exhibited the highest power density, while the acid-treated and commercial catalyst showed comparable power density. Durability was also tested in a single-cell by repeating CVs in 0.6–1.0 V at 100 mV s^{-1} for 30,000 cycles with a feed of 200 sccm H_2 in the anode and 75 sccm Ar in the cathode with 100% RH. The current densities after the durability test were 0.07, 0.16, and 0.04 A cm^{-2} at 0.8 V, and 0.81, 1.40, and 0.63 A cm^{-2} at 0.6 V for the acid-treated, Au-doped, and commercial Pt catalysts, respectively. The maximum power densities after the durability test were 0.68, 1.12, and 0.69 W cm^{-2} for the acid-treated, Au-doped, and commercial Pt catalysts, respectively. The effect of Au doping was more evident after the durability test. Fig. 6 shows TEM images of the catalysts after the durability test. While the particle size increased greatly to 14.7 ± 12.3 nm for the acid-treated catalyst, the particles in the Au-doped catalyst increased less, to 8.1 ± 3.0 nm. Cross-sectional SEM and EDS-mapping images are also shown in Fig. 6. The blue dots in the mapping images indicate Co atoms, showing that Co was transferred into the membrane much more in the acid-treated catalyst than in the Au-doped catalyst. The overall composition was 94% Pt and 6% Co for the acid-treated catalyst while

the values were 87% Pt, 12% Co, and 1% Au. Clearly, Co was leached much less in the presence of Au even in the single-cell tests. The surface Pt was more metallic in the presence of Au after the durability test, similar to the half-cell case. The durability was tested again in much harsher condition for Au-doped PtCo catalyst; 0.6–1.3 V for half-cell test (Figure S9) and 0.6–1.2 V for single-cell test (Figure S10). It was found that the performance was degraded and the nanoparticles were aggregated significantly.

3.3. DFT calculations

To understand the role of Au in the Au-doped PtCo catalyst for ORR activity and durability, DFT calculations were conducted. First, the oxygen binding energy (E_b) was calculated at the surface of pure Pt, PtCo, and Au-doped PtCo slabs. Because acid-treated Pt alloy catalysts typically have pure Pt layers at the surface [55,56], the model structure for acid-treated PtCo catalyst was constructed with pure Pt skinlayers supported on a PtCo (110) substrate. Oxygen binding energy has been used as a key descriptor representing the ORR activity of metal-based catalysts [57,58]. The E_b is defined as follows.

$$E_b = E_{slab/O} - E_{slab} - E_O$$

where $E_{slab/O}$, E_{slab}, and E_O indicate the total energy of the slab on which atomic O was adsorbed, a clean slab, and the gas-phase O system, respectively. As shown in Fig. 7, spin-polarized DFT calculations predict that the oxygen binding energy is weaker in the ordered PtCo (-4.45 eV) or Au-doped PtCo (-4.41 eV) than pure Pt (-4.71 eV). The oxygen affinity is reduced on the PtCo and reduced even further on the Au-doped PtCo. It is known that lower oxygen binding energy can accelerate the rate-limiting step of the ORR, which is the removal of dissociated O adsorbed at the surface by protonation [59]. The decrease in the oxygen binding energy would cause an enhancement in ORR activity for the PtCo or Au-doped PtCo catalysts.

Next, Co segregation energy was evaluated for the migration of a Co atom from the inside toward the surface, to examine the durability of the catalysts. The segregation energy is defined as follows.

$$\Delta E_{n \to n-1}^{clean(or\ oxygen)} = E_{n-1}^{clean(or\ oxygen)} - E_n^{clean(or\ oxygen)}$$

where n is the vertical position of a Co atom in the atomic layer of the PtCo or Au-doped PtCo slab (for example, n = 2 indicates the presence of a Co atom in the second layer), $E_n^{clean(or\ oxygen)}$ is the total energy of the PtCo or Au-doped PtCo slab when the Co atom is located at the nth layer under the clean or oxygen-adsorbed condition, and $\Delta E_{n \to n-1}^{clean(or\ oxygen)}$ is the segregation energy for the migration of a Co atom in the nth layer toward the n-1th layer. Fig. 8 shows the segregation energy calculated for the migration of a Co atom from the 4th layer to the upper layers. A positive value of ΔE indicates that the surface migration of Co is not favored, while a negative value indicates that the migration is favored [60]. For the PtCo catalyst, $\Delta E_{4 \to 3}^{clean}$, $\Delta E_{3 \to 2}^{clean}$, and $\Delta E_{2 \to 1}^{clean}$ values were -0.03, -0.08, and + 0.35 eV, respectively, with $\Delta E_{4 \to 1}^{clean}$ of + 0.24 eV. The Co migration to the surface was not favored for the clean PtCo catalyst. However, the $\Delta E_{4 \to 3}^{oxygen}$, $\Delta E_{3 \to 2}^{oxygen}$, and $\Delta E_{2 \to 1}^{oxygen}$ values changed to -0.67, + 0.41, and + 0.10 eV, respectively, with $\Delta E_{4 \to 1}^{oxygen}$ of -0.16 eV in the presence of oxygen adsorbed at the surface. The Co migration to the surface was favored when oxygen intermediates were adsorbed at the surface. This suggests that the acid-treated PtCo catalyst will suffer from a gradual loss of Co during the ORR. For the Au-doped PtCo catalyst, $\Delta E_{4 \to 3}^{clean}$, $\Delta E_{3 \to 2}^{clean}$, and $\Delta E_{2 \to 1}^{clean}$ values were + 0.08, + 0.09, and + 0.50 eV, respectively, with $\Delta E_{4 \to 1}^{clean}$ of + 0.67 eV. The $\Delta E_{4 \to 3}^{oxygen}$, $\Delta E_{3 \to 2}^{oxygen}$, and $\Delta E_{2 \to 1}^{oxygen}$ values changed to + 0.14, + 0.10, and + 0.25 eV, respectively, with $\Delta E_{4 \to 1}^{oxygen}$ of + 0.49 eV in the presence of oxygen adsorbed at the surface. The Co migration to the surface was not favored in the absence or presence of surface oxygen species. Clearly, Au-doping can suppress the Co leaching during the ORR, enhancing the durability of the catalyst. The Au-doped PtCo catalyst showed enhanced activity and durability for the ORR because the Au-doping weakens the binding of surface oxygen species on the surface and suppresses Co leaching during the ORR.

4. Conclusion

Au-doped PtCo/C catalyst was prepared in a gram-scale by gas-phase reduction and subsequent galvanic replacement. The overall atomic composition of the catalyst measured by ICP was 74% Pt, 24% Co, and 2% Au, while the surface composition measured by XPS was 82% Pt, 17% Co, and 1% Au. When the mass activity was compared per unit mass of Pt + Au in a half-cell, the current density of the Au-doped PtCo/C catalyst at 0.9 V_{RHE} was 0.81 A mg_{PGM}^{-1}, while the values for the acid-treated PtCo/C and commercial Pt/C catalysts were 0.52 and 0.23 A mg_{PGM}^{-1}, respectively. More importantly, the activity and durability of the Au-doped PtCo/C catalyst was tested in a single-cell. The current density of the Au-doped PtCo/C catalyst at 0.6 V was 1.63 A cm^{-2}, while the values for the acid-treated PtCo/C and commercial Pt/C catalysts were 1.31 and 1.20 A cm^{-2} when the same mass of Pt (0.2 mg/cm^{-2}) were loaded on the cathode. After the durability test, which was conducted by repeating CVs in 0.6–1.0 V for 30,000 cycles at 100 mV s^{-1}, the current densities at 0.6 V decreased to 1.40, 0.81, and 0.63 A cm^{-2}. The Au-doped PtCo/C showed durability superior to acid-treated PtCo/C or commercial Pt/C. DFT calculations showed that Au-doping weakened the binding of surface oxygen species on the surface and suppressed Co leaching. This method provides a facile way to enhance the activity and durability of the electrode catalyst for PEMFC application.

Appendix A. Supplementary data

Supplementary material related to this article can be found, in the online version, at doi:https://doi.org/10.1016/j.apcatb.2019.02.002.

References

[1] C. Kim, J.-G. Oh, Y.-T. Kim, H. Kim, H. Lee, Electrochem. Commun. 12 (2010) 1596–1599.
[2] D.H. Kwak, S.B. Han, Y.W. Lee, H.S. Park, I.A. Choi, K.B. Ma, M.C. Kim, S.J. Kim, D.H. Kim, J.I. Sohn, K.W. Park, Appl. Catal. B: Environ. 203 (2017) 889–898.
[3] R.A.M. Esfahani, R.B. Moghaddam, I.I. Ebralidze, E.B. Easton, Appl. Catal. B: Environ. 239 (2018) 125–132.
[4] A. Serov, A.D. Shum, X.H. Xiao, V. De Andrade, K. Artyushkova, I.V. Zenyuk, P. Atanassov, Appl. Catal. B: Environ. 237 (2018) 1139–1147.
[5] M. Chen, B. Wu, J. Yang, N. Zheng, Adv. Mater. 24 (2012) 862–879.
[6] C. Kim, S.S. Kim, S. Yang, J.W. Han, H. Lee, Chem. Commun. 48 (2012) 6396–6398.
[7] J. Wu, L. Qi, H. You, A. Gross, J. Li, H. Yang, J. Am. Chem. Soc. 134 (2012) 11880–11883.
[8] S.I. Choi, S. Xie, M. Shao, J.H. Odell, N. Lu, H.C. Peng, L. Protsailo, S. Guerrero, J. Park, X. Xia, J. Wang, M.J. Kim, Y. Xia, Nano Lett. 13 (2013) 3420–3425.
[9] H.A. Gasteiger, S.S. Kocha, B. Sompalli, F.T. Wagner, Appl. Catal. B: Environ. 56 (2005) 9–35.
[10] M. Ammam, E.B. Easton, J. Power Sources 236 (2013) 311–320.
[11] J. Choi, Y. Lee, J. Kim, H. Lee, J. Power Sources 307 (2016) 883–890.
[12] J. Kim, S. Yang, H. Lee, Electrochem. Commun. 66 (2016) 66–70.
[13] E. Antolini, Appl. Catal. B: Environ. 217 (2017) 201–213.
[14] X. Peng, S. Zhao, T.J. Omasta, J.M. Roller, W.E. Mustain, Appl. Catal. B: Environ. 203 (2017) 927–935.
[15] N.E. Sahin, T.W. Napporn, L. Dubau, F. Kadirgan, J.M. Leger, K.B. Kokoh, Appl. Catal. B: Environ. 203 (2017) 72–84.
[16] J. Choi, J.-H. Jang, C.-W. Roh, S. Yang, J. Kim, J. Lim, S.J. Yoo, H. Lee, Appl. Catal. B: Environ. 225 (2018) 530–537.
[17] H. Park, K.M. Kim, H. Kim, D.-K. Kim, Y.S. Won, S.-K. Kim, Korean J. Chem. Eng. 35 (2018) 1547–1555.

[18] J. Ying, J. Li, G.P. Jiang, Z.P. Cano, Z. Ma, C. Zhong, D. Su, Z.W. Chen, Appl. Catal. B: Environ. 225 (2018) 496–503.

[19] J.R. Kitchin, J.K. Norskov, M.A. Barteau, J.G. Chen, J. Chem. Phys. 120 (2004) 10240–10246.

[20] J.R. Kitchin, J.K. Norskov, M.A. Barteau, J.G. Chen, Phys. Rev. Lett. 93 (2004) 156801.

[21] V.V. Stamenkovic, B.S. Mun, K.J.J. Mayrhofer, P.N. Ross, N.M. Markovic, J. Rossmeisl, J. Greeley, J.K. Nørskov, Angew. Chem. Int. Ed. 118 (2006) 2963–2967.

[22] V.R. Stamenkovic, B.S. Mun, M. Arenz, K.J. Mayrhofer, C.A. Lucas, G. Wang, P.N. Ross, N.M. Markovic, Nat. Mater. 6 (2007) 241–247.

[23] J. Shin, J.H. Choi, P.R. Cha, S.K. Kim, I. Kim, S.C. Lee, D.S. Jeong, Nanoscale 7 (2015) 15830–15839.

[24] U.A. Paulus, A. Wokaun, G.G. Scherer, T.J. Schmidt, V. Stamenkovic, V. Radmilovic, N.M. Markovic, P.N. Ross, J. Phys. Chem. B 106 (2002) 4181–4191.

[25] E. Antolini, J. Salgado, M. Giz, E. Gonzalez, Int. J. Hydrogen Energy 30 (2005) 1213–1220.

[26] E. Antolini, J.R.C. Salgado, E.R. Gonzalez, J. Power Sources 160 (2006) 957–968.

[27] M. Oezaslan, P. Strasser, J. Power Sources 196 (2011) 5240–5249.

[28] D. Wang, H.L. Xin, R. Hovden, H. Wang, Y. Yu, D.A. Muller, F.J. DiSalvo, H.D. Abruna, Nat. Mater. 12 (2013) 81–87.

[29] A. Kongkanand, M.F. Mathias, J. Phys. Chem. Lett. 7 (2016) 1127–1137.

[30] N. Konno, S. Mizuno, H. Nakaji, Y. Ishikawa, SAE Int. J. Alter. Powertrains 4 (2015) 123–129.

[31] M.J. Kelly, G. Fafilek, J.O. Besenhard, H. Kronberger, G.E. Nauer, J. Power Sources 145 (2005) 249–252.

[32] S. Koh, P. Strasser, J. Am. Chem. Soc. 129 (2007) 12624–12625.

[33] S. Koh, M.F. Toney, P. Strasser, Electrochim. Acta 52 (2007) 2765–2774.

[34] P. Mani, R. Srivastava, P. Strasser, J. Phys. Chem. C 112 (2008) 2770–2778.

[35] R.R. Adzic, J. Zhang, K. Sasaki, M.B. Vukmirovic, M. Shao, J.X. Wang, A.U. Nilekar, M. Mavrikakis, J.A. Valerio, F. Uribe, Top. Catal. 46 (2007) 249–262.

[36] K.A. Kuttiyiel, K. Sasaki, Y. Choi, D. Su, P. Liu, R.R. Adzic, Energy Environ. Sci. 5 (2012) 5297–5304.

[37] F.H.B. Lima, J. Zhang, M.H. Shao, K. Sasaki, M.B. Vukmirovic, E.A. Ticianelli, R.R. Adzic, J. Solid State Electrochem. 12 (2007) 399–407.

[38] J. Zhang, Y. Mo, M.B. Vukmirovic, R. Klie, K. Sasaki, R.R. Adzic, J. Phys. Chem. B 108 (2004) 10955–10964.

[39] Y. Ma, P.B. Balbuena, Surf. Sci. 602 (2008) 107–113.

[40] G.E. Ramirez-Caballero, Y. Ma, R. Callejas-Tovar, P.B. Balbuena, Phys. Chem. Chem. Phys. 12 (2010) 2209–2218.

[41] M. Kettner, W.B. Schneider, A.A. Auer, J. Phys. Chem. C 116 (2012) 15432–15438.

[42] J. Zhang, K. Sasaki, E. Sutter, R.R. Adzic, Science 315 (2007) 220–222.

[43] A. Dorjgotov, Y. Jeon, J. Hwang, B. Ulziidelger, H.S. Kim, B. Han, Y.G. Shul, Electrochim. Acta 228 (2017) 389–397.

[44] M. Gatalo, P. Jovanovič, G. Polymeros, J.-P. Grote, A. Pavlišič, F. Ruiz- Zepeda, V.S. Šelih, M. Šala, S. Hočevar, M. Bele, K.J.J. Mayrhofer, N. Hodnik, M. Gaberšček, ACS Catal. 6 (2016) 1630–1634.

[45] Y. Kang, J. Snyder, M. Chi, D. Li, K.L. More, N.M. Markovic, V.R. Stamenkovic, Nano Lett. 14 (2014) 6361–6367.

[46] L.-L. Shen, G.-R. Zhang, S. Miao, J. Liu, B.-Q. Xu, ACS Catal. 6 (2016) 1680–1690.

[47] Q. Shi, C. Zhu, S. Fu, D. Du, Y. Lin, ACS Appl. Mater. Interfaces 8 (2016) 4739–4744.

[48] G.F. Kresse, J. Furthmuller, VASP the Guide, Vienna Universit of Technology, Vienna, Austria, 2001.

[49] J.P. Perdew, K. Burke, M. Ernzerhof, Phys. Rev. Lett. 77 (1996) 3865–3868.

[50] P.E. Blochl, Phys. Rev. B 50 (1994) 17953–17979.

[51] P.E. Blöchl, O. Jepsen, O.K. Andersen, Phys. Rev. B. 49 (1994) 16223–16233.

[52] V. Di Noto, E. Negro, S. Polizzi, F. Agresti, G.A. Giffin, ChemSusChem 5 (2012) 2451–2459.

[53] Q. Jia, K. Caldwell, D.E. Ramaker, J.M. Ziegelbauer, Z. Liu, Z. Yu, M. Trahan, S. Mukerjee, J. Phys. Chem. C 118 (2014) 20496–20503.

[54] M.K. Debe, Nature 486 (2012) 43–51.

[55] K. Zhang, Q.L. Yue, G.F. Chen, Y.L. Zhai, L. Wang, H.S. Wang, J.S. Zhao, J.F. Liu, J.B. Jia, H.B. Li, J. Phys. Chem. C 115 (2011) 379–389.

[56] B. Patrick, H.C. Ham, Y. Shao-Horn, L.F. Allard, G.S. Hwang, P.J. Ferreira, Chem. Mater. 25 (2013) 530–535.

[57] C.E. Kim, D.H. Lim, J.H. Jang, H.J. Kim, S.P. Yoon, J. Han, S.W. Nam, S.A. Hong, A. Soon, H.C. Ham, J. Chem. Phys. 142 (2015) 034707.

[58] L. Ou, S. Chen, J. Phys. Chem. C 117 (2013) 1342–1349.

[59] J.K. Norskov, J. Rossmeisl, A. Logadottir, L. Lindqvist, J.R. Kitchin, T. Bligaard, H. Jonsson, J. Phys. Chem. B 108 (2004) 17886–17892.

[60] H.C. Ham, D. Manogaran, K.H. Lee, K. Kwon, S.A. Jin, D.J. You, C. Pak, G.S. Hwang, J. Chem. Phys. 139 (2013) 201104.